

Local field correction to ionization potential depression of ions in warm or hot dense matterXiaolei Zan ¹, Chengliang Lin,^{2,*} Yong Hou ^{1,†} and Jianmin Yuan ^{2,1,‡}¹*Department of Physics, College of Liberal Arts and Sciences, National University of Defense Technology, Changsha, Hunan 410073, People's Republic of China*²*Graduate School of China Academy of Engineering Physics, Beijing 100193, People's Republic of China*

(Received 13 April 2021; accepted 19 July 2021; published 9 August 2021)

An analytical self-consistent approach was recently established to predict the ionization potential depression (IPD) in multicomponent dense plasmas, which is achieved by considering the self-energy of ions and electrons within the quantum statistical theory. In order to explicitly account for the exchange-correlation effect of electrons, we incorporate the effective static approximation of local field correction (LFC) within our IPD framework through the connection of dynamical structure factor. The effective static approximation poses an accurate description for the asymptotic large wave number behavior with the recently developed machine learning representation of static LFC induced from the path-integral Monte Carlo data. Our calculation shows that the introduction of static LFC through dynamical structure factor brings a nontrivial influence on IPD at warm/hot dense matter conditions. The correlation effect within static LFC could provide up to 20% correction to free-electron contribution of IPD in the strong coupling and degeneracy regime. Furthermore, a new screening factor is obtained from the density distribution of free electrons calculated within the average-atom model, with which excellent agreements are observed with other methods and experiments at warm/hot dense matter conditions.

DOI: [10.1103/PhysRevE.104.025203](https://doi.org/10.1103/PhysRevE.104.025203)**I. INTRODUCTION**

In a many-body environment, the properties of a bound electron are not only affected by its nucleus and other bound electrons, but also by the surrounding free electrons and other neighboring ions. For dense plasma systems, a well-known phenomenon among these properties is the ionization potential depression (IPD). Detailed knowledge of IPD is of essential importance for the description of physical processes related to bound-free transitions, since the ionization balance [1–3] and also rate coefficients [4–7] are significantly altered by the IPD. Therefore, accurate prediction of IPD plays a key role for determination of the thermodynamic and optical properties of the plasma system and for fully understanding a wide range of atomic processes within plasma environments [8], i.e., for studies on warm dense matter (WDM) [9,10] such as shock experiments [11,12], planetary science [13,14], inertial confinement fusion [15,16], and nonequilibrium plasmas created with x-ray free-electron lasers [17,18].

In the last few years, the rapid development of high-intense laser facilities [19–23] makes it possible to access precise and valuable experiment data on IPD under extreme conditions in the high energy density regime [24–26]. The experimental outcomes can be used to benchmark the IPD models and the associate physical assumptions. Comparison of the experimental observation to the widespread Ecker and Kröll

(EK) [27] and Stewart and Pyatt (SP) [28] models reveals the invalidity of these analytic models, since these models always fail to correctly describe the effective screening length as well as the structure of dense plasmas and therefore, usually break down one way or another. Theoretical methods beyond the classical analytic models, including the two-step Hartree-Fock-Slater model [29], density functional theory molecular dynamics [30,31], Monte Carlo method [32], the fluctuation model [33], and atomic-solid-plasma model [34], have had great success in explaining the new experiment results. More recently, a consistent approach is developed to determine the screening potential in dense plasmas, whereby the IPD information is also obtained simultaneously [3,35]. Furthermore, a nonlocal thermal equilibrium approach by combining a quantum-mechanical electronic-structure calculation and a Monte Carlo molecular-dynamics simulation has been proposed to calculate the IPD effect under nonthermal situations [36]. These state-of-the-art methods indicate that the trend in IPD prediction gradually transforms into the combination of theoretical modeling with *ab initio* simulation.

Based on the quantum statistical theory, an analytical self-consistent approach was established for the IPD effect [37,38], and had been extended to describe the realistic multicomponent mixture [39]. Investigation on different chemical elements in a wide range of temperatures and densities displayed good agreements between theoretical predictions and the corresponding experiments. However, in the previous study the Debye-Hückel (DH) model is employed to describe the electron-electron response, which only becomes valid in the low-density and the high temperature limits. At WDM conditions, the intricate interplay of Coulomb correlations,

*cclin@gscaep.ac.cn

†yonghou@nudt.edu.cn

‡jmyuan@gscaep.ac.cn; jmyuan@nudt.edu.cn

thermal excitations, and quantum exchange effects makes theoretical modeling for WDM systems very challenging. In particular, an accurate description of an electronic subsystem is of essential relevance at WDM conditions, in which case the DH model for electron-electron response is inadequate to capture dynamical properties of electrons. To incorporate dynamical correlations as well as quantum degeneracy effects into the previously proposed IPD model, more advanced response function for electrons is necessary.

Therefore, performing research to fill this gap is of great practical significance for matters under WDM conditions. To accomplish this goal, local field correction (LFC) is introduced to account for the correlation effects in the present work. Including the LFC in the density response function of collisionless electron gas provides a way to describe the exchange and correlation effects between electrons. The connection of exchange-correlation effects, LFC, and other related quantities within uniform electron gases at WDM conditions is recently studied in detail in Refs. [40–48] based on the quantum Monte Carlo (QMC) simulations. In this work, a machine learning representation of static LFC [49] is utilized to calculate the electronic dynamical structure factor, which is an essential ingredient of the proposed IPD model. In this way, the electronic exchange-correlation effects is fully accounted in our proposed approach. As demonstrated in this paper, a nontrivial influence is discovered by introducing the LFC on IPD at WDM conditions. The correlation effect of free electrons introduced by static LFC could provide up to 20% correction to free-electron contribution of IPD in the strong coupling and degeneracy regime.

The present work is organized as follows: In Sec. II A, we outline the approach for our calculation and describe the relation between IPD and structure factor (SF); in Sec. II B, we review different approaches to obtain the static SF of free electrons as well as the LFC involved in the calculation of SF; in Sec. II C, we focus on the ionic SF and screening function. In Sec. III A, we show the influence of LFC and dynamical effect on the free-electron contribution to IPD. Then, we calculate the IPD at moderate coupling and nondegenerate region (Sec. III B) and strong coupling and degenerate region (Sec. III C). Finally, conclusions are drawn in Sec. IV.

II. METHODS

A. Quantum statistical framework for the determination of IPD

The physical system investigated in the present work is a multicomponent mixture constructed of N_e free electrons and N_α ions with charge z_α in a box with volume V . The partial particle number density is defined as $n_c = N_c/V$ with $c = e, \alpha$. The change of the ionization potential (IP) of an atomic/ionic system with charge z_α in a plasma environment in comparison to that of the corresponding isolated case is described by IPD, which is defined as

$$\mathcal{I}_\alpha^{\text{IPD}} = \text{IP}_\alpha^{\text{env}} - \text{IP}_\alpha^{\text{iso}}, \quad (1)$$

where $\text{IP}_\alpha^{\text{iso}} = E_\alpha^{\text{iso}} - E_{\alpha+1}^{\text{iso}}$ is the IP in the isolated system, E_α^{iso} is the total energy of isolated ion α ; $\text{IP}_\alpha^{\text{env}} = E_\alpha^{\text{env}} - E_{\alpha+1}^{\text{env}} - \Sigma_e$ is the IP in a plasma environment, where $E_\alpha^{\text{env}} = E_\alpha^{\text{iso}} + \Sigma_\alpha$ is the total energy of ion α in a plasma environment. Σ_α is the

self-energy (SE) of ion α , which describes the influence of the surrounding environment, including free electrons and other neighboring ions, on the ionized ion. Accordingly, the total energy of the involved electron is Σ_e . Then it is straightforward to express the IPD in terms of self-energy

$$\begin{aligned} \mathcal{I}_\alpha^{\text{IPD}} &= (E_\alpha^{\text{env}} - E_\alpha^{\text{iso}}) - (E_{\alpha+1}^{\text{env}} - E_{\alpha+1}^{\text{iso}}) - \Sigma_e \\ &= \Sigma_\alpha - \Sigma_{\alpha+1} - \Sigma_e. \end{aligned} \quad (2)$$

In the framework of the Green's function method, the self-energy of ion α can be further divided into the Hartree-Fock (HF) term $\Sigma_\alpha^{\text{HF}}$ and correlation term $\Sigma_\alpha^{\text{corr}}$, which describe the quantum exchange effect and dynamical correlation effect between ion α and other particles, respectively. In the warm/hot dense regime, correlation term $\Sigma_\alpha^{\text{corr}}$ plays an important role. In the remainder of this work, we concentrate on the dynamical correlation effect to the IPD. Within the G_0W approximation, the resulting dynamical correlation contribution to the IPD can be expressed as an integral of the dielectric function of the system

$$\begin{aligned} \mathcal{I}_\alpha^{\text{dc}} &= \Sigma_\alpha^{\text{corr}} - \Sigma_{\alpha+1}^{\text{corr}} - \Sigma_e^{\text{corr}} \\ &= \int \frac{d^3\mathbf{k}}{(2\pi)^3} \int_{-\infty}^{\infty} \frac{d\omega_2}{2\pi} \frac{2(z_\alpha + 1)e^2}{\varepsilon_0 k^2 \omega_2} \text{Im} \left[\frac{n_B(\omega_2) + 1}{\varepsilon(\mathbf{k}, \omega_2)} \right] \end{aligned} \quad (3)$$

with $n_B(\omega) = 1/(\exp[\beta(\hbar\omega - \mu)] - 1)$ the Bose-distribution function. According to the fluctuation-dissipation theorem, the effective charge-charge response to an external perturbation, i.e., $\varepsilon(\mathbf{k}, \omega)$, can be represented in terms of the charge-charge dynamical SF $S_{ZZ}(\mathbf{k}, \omega)$,

$$\text{Im} \left[\frac{n_B(\omega) + 1}{\varepsilon(\mathbf{k}, \omega)} \right] = \frac{\pi k_B T}{\hbar k^2} \kappa_{\text{scr}}^2 S_{ZZ}(\mathbf{k}, \omega). \quad (4)$$

The total charge-charge dynamical SF $S_{ZZ}(\mathbf{k}, \omega)$ consists of two parts: the dynamical SF of free electrons $S_{ee}^0(\mathbf{k}, \omega)$ and effective ionic charge-charge dynamical SF $S_{ZZ}^{\text{ion}}(\mathbf{k}, \omega)$:

$$S_{ZZ}(\mathbf{k}, \omega) = \frac{1}{1 + z_p} S_{ee}^0(\mathbf{k}, \omega) + \frac{z_p}{1 + z_p} S_{ZZ}^{\text{ion}}(\mathbf{k}, \omega). \quad (5)$$

All the complexity in the plasma environment, including the dynamical impact on the electronic dynamical SF $S_{ee}(\mathbf{k}, \omega)$ due to the attraction of ions and the electron-ion dynamical SF $S_{ey}(\mathbf{k}, \omega)$, are all contained in the latter contribution $S_{ZZ}^{\text{ion}}(\mathbf{k}, \omega)$.

Combining Eqs. (3)–(5), we finally arrive at a practical form for the dynamical correlation contribution to the IPD:

$$\mathcal{I}_\alpha^{\text{dc}} = \frac{1}{1 + z_p} \mathcal{I}_\alpha^{\text{dc,el}} + \frac{z_p}{1 + z_p} \mathcal{I}_\alpha^{\text{dc,ion}}, \quad (6)$$

with the free-electron contribution:

$$\mathcal{I}_\alpha^{\text{dc,el}} = \frac{(z_\alpha + 1)e^2 \kappa_{\text{eff}}^2 a_0}{2\pi^2 \varepsilon_0 r_\alpha^2} \int_0^\infty \frac{dk_0}{k_0^2} S_{ee}^0(k_0), \quad (7)$$

and the screened ionic contribution:

$$\mathcal{I}_\alpha^{\text{dc,ion}} = \frac{(z_\alpha + 1)e^2 \kappa_{\text{eff}}^2 a_0}{2\pi^2 \varepsilon_0 r_\alpha^2} \int_0^\infty \frac{dk_0}{k_0^2} S_{ZZ}^{\text{ion}}(k_0), \quad (8)$$

with $k_0 = ka_0$ in terms of the Bohr radius a_0 . κ_{eff} is the effective inverse screening parameter and $r_\alpha = [3(z_\alpha + 1)/(4\pi n_e)]^{1/3}$ is the ionic radius.

As a direct consequence of the decomposition in Eq. (5), the total IPD is also divided into two corresponding components. The free-electron part only covers the influence of the dynamic response induced by the fast oscillating electrons. The slowly moving part of the surrounding plasma environment is included in the screened ionic contribution, which describes the ion-ion correlation as well as the electron-ion screening effect within the plasmas. In this way, a direct connection between the IPD and the SF of the plasma system is established. Another advantage of the currently proposed model is the decomposition of the screened ionic and the free-electron contribution. Such splitting makes it convenient for us to investigate different physical effects on IPD and to benchmark the validity of different approximations, which will be discussed in detail in the subsequent sections.

B. Structure factor of free electrons and local field correction

In dense plasma systems, electron-electron static response can be characterized by the static SF of electrons. Reasonable and accurate evaluation of static SF for warm dense electron systems is still an ongoing research theme. In the nondegenerate and weakly coupling regime, the electron-electron response can be calculated on the basis of the Debye-Hückel theory, which leads to the Debye-Hückel form for the static SF of free electrons

$$S_{ee}^0(k) = \frac{k^2}{k^2 + \kappa_e^2}, \quad (9)$$

where κ_e is the inverse of the electron Debye length. With the increase of the electron coupling parameter, strong correlations between free electrons can be accounted for by modifying the bare Coulomb potential with LFC. In the WDM regime, however, the Debye-Hückel SF (9) and its modified version with the LFC extension cannot catch the quantum exchange effect and dynamical correlation effect within the electron gas systems.

The static SF can be also obtained via integrating out the frequency in the dynamical SF

$$S_{ee}^0(k) = \int_{-\infty}^{\infty} d\omega S_{ee}^0(k, \omega). \quad (10)$$

After the frequency integration of $S_{ee}^0(k, \omega)$, the influence of dynamical effects remains compared with the above static models. The dynamical SF is defined as the Fourier transform of density-density correlation function $\langle \rho(\mathbf{k}, t) \rho(-\mathbf{k}, 0) \rangle$. In the linear response theory, $S_{ee}^0(k, \omega)$ can be obtained from dynamical density-response function of free electrons $\chi_{ee}^0(k, \omega)$ given by the fluctuation-dissipation theorem:

$$S_{ee}^0(k, \omega) = -\frac{\text{Im}\chi_{ee}^0(k, \omega)}{\pi n_e(1 - e^{-\beta\omega})}, \quad (11)$$

and the dynamical density-response function reads

$$\chi_{ee}^0(k, \omega) = \frac{\chi_0(k, \omega)}{1 - V_{ee}(k)[1 - G(k, \omega)]\chi_0(k, \omega)}, \quad (12)$$

with the Lindhard density-response function of the noninteracting system $\chi_0(k, \omega)$ and the dynamical LFC $G(k, \omega)$. The response function $\chi_{ee}^0(k, \omega)$ in the well-known random phase approximation (RPA) is recovered by ignoring the dynamical LFC. The essential problem going beyond the RPA result is to determine the dynamical LFC $G(k, \omega)$ with high accuracy. In this work, we perform Monte Carlo simulation to obtain the SF of free electrons. It is demonstrated that the QMC method is able to accurately describe the behavior of SFs from ground state to classical Debye-Hückel limits for warm dense homogeneous electron gas [41]. Combining with the Singwi-Tosi-Land-Sjölander approximation [50–52], path-integral Monte Carlo (PIMC) simulations can also provide the static SF of free electrons over the entire k range [47].

In the PIMC simulation, the imaginary-time density correlation function $\langle \rho(\mathbf{k}, \tau) \rho(-\mathbf{k}, 0) \rangle$ (with $\tau = -i\hbar\beta$) is directly evaluated. The dynamical SF is then acquired in terms of the inverse Laplace transform of the imaginary-time correlation function. As pointed out by Groth *et al.* [44], numerical implementation of the inverse Laplace transform connecting the dynamical SF $S_{ee}^0(k, \omega)$ and the imaginary-time density correlation function is an ill-posed problem due to the statistical uncertainty in the corresponding QMC data. Instead of an immediate evaluation of the dynamical SF through inverse Laplace transform, one can also calculate the dynamical LFC $G(k, \omega)$, which provides additional constraints for the reconstruction of the dynamical SF from the QMC data. Such procedure for determination of dynamical SF is developed by Dornheim *et al.* [48], where trial solutions $G_{\text{trial}}(k, \omega)$ that satisfy the symmetry properties and also different asymptotic limits of the dynamical LFC are stochastically selected. Once the final $G(k, \omega)$ is picked out according to the PIMC data, the corresponding dynamical SF is obtained by Eqs. (11) and (12).

A further simplification for the LFC of the response function is to take the static version of the dynamical LFC $G(k) = G(k, 0)$. The static LFC $G(k)$ can be obtained directly from PIMC data. Based on an extensive set of PIMC and CDOP data [53], Dornheim *et al.* finally included 6.5×10^4 $G(k)$ samples into their training set to train a fully connected deep neural network (40 hidden layers with 64 neurons each), and achieved a machine learning representation of $G(k; r_s, \theta)$ with respect to continuous wave vectors, densities, and temperatures over the entire WDM regime [49]. Moreover, in order to correctly describe the large wave number limit of static LFC $G(k)$, accurate asymptotic expression is added into the above machine learning representation. Such combination leads to the effective static approximation (ESA) for the LFC of free electrons [45]. In the majority of the WDM regime, the dynamical SF $S_{ee}^0(k, \omega)$ based on the static LFC $G(k)$ is manifested to be adequate for most calculations [48] to capture the impact of dynamical correlation within the warm dense systems. To investigate the dynamical effects and short-range correlation effects of the electronic subsystem, we will apply the ESA version of static LFC to calculate the dynamical SF $S_{ee}^0(k, \omega)$ of free electrons. The corresponding static SF is established by integration over the frequency variable of the resulting $S_{ee}^0(k, \omega)$.

C. Effective ionic charge-charge structure factor and screening function

The effective ionic charge-charge SF $S_{ZZ}^{\text{ion}}(k)$ describes the ionic correlation and the electron screening effect on the ions. It includes the ion-ion SF and the electron-ion partial SF and can be expressed in terms of the ionic density-density SF $S_{\alpha\beta}(k)$ of ion α and β multiplied by a screening function,

$$S_{ZZ}^{\text{ion}}(k) = [1 - q_{\text{scr}}(k)]^2 \sum_{\alpha\beta} \frac{z_{\alpha}z_{\beta}\sqrt{x_{\alpha}x_{\beta}}}{\bar{z}z_p} S_{\alpha\beta}(k). \quad (13)$$

The static SF $S_{\alpha\beta}(k)$ can be computed from the pair distribution function in the hypernetted chain (HNC) approximation [54–56] as well as other numerical simulations such as molecular dynamic simulation. $q_{\text{scr}}(k)$ represents the correlation between free and bound electrons and takes the following form in the framework of linear response theory:

$$q_{\text{scr}}(k) = \frac{V_{e\alpha}(k)[1 - \varepsilon_{ee}(k, 0)]}{z_{\alpha}V_{ee}(k)\varepsilon_{ee}(k, 0)} = \frac{\varepsilon_{ee}(k, 0) - 1}{\varepsilon_{ee}(k, 0)}. \quad (14)$$

In the long-wavelength limit, the dielectric function has the form $\varepsilon_{ee}(k, 0) = 1 + (\kappa_e/k)^2$, which results in the Debye-Hückel expression for the screening function

$$q_{\text{scr}}^{\text{DH}}(k) = \frac{q_{\alpha}(k)}{z_{\alpha}} = \frac{\kappa_e^2}{k^2 + \kappa_e^2}. \quad (15)$$

The validity of this expression is restricted to the weakly coupled plasma systems. For moderately and strongly coupled warm dense plasmas, more advanced expression for the dielectric function of free electrons has to be utilized:

$$\varepsilon_{ee}(k, 0) = 1 - \frac{V_{ee}(k)\chi_0(k, 0)}{1 + V_{ee}(k)G(k)\chi_0(k, 0)}, \quad (16)$$

where the static LFC $G(k)$ can be obtained with the machine learning representation. Neglecting the static LFC $G(k)$ leads to the RPA version of screening function.

The screening factor can be also obtained from the detailed information of the electronic wave functions through solving the Dirac equation with some effective potentials. Within the average-atom (AA) model, we can calculate the screening factor from the free-electron density distribution of each ionic Wigner-Seitz sphere [56–59],

$$q_{\text{scr}}(k) = \frac{4\pi}{z_{\alpha}k} \int_0^{r_{\alpha}} dr r \sin(kr) \rho_e(r). \quad (17)$$

To compare the screening factors $[1 - q_{\text{scr}}(k)]^2$ calculated within different approximations, we take Al^{3+} plasma at $\rho = 2.7 \text{ g cm}^{-3}$ and $t = 10 \text{ eV}$ as an example. In Fig. 1 the results for the screening factors $[1 - q_{\text{scr}}(k)]^2$ obtained from the long-wavelength formula, RPA, ESA, and AA models are shown. The screening factors within the RPA and ESA are generally in good agreement, while the deviation of long-wavelength formula in the large wave number region is relatively large. It can be seen that the AA model predicts an oscillating structure for the screening factors around the RPA and ESA results. With the help of LFC, the screening factor obtained by ESA comes closer to that of the AA model in the small wave number region. The oscillation in the middle to large wave number region corresponds to the inner-shell-electron structure with large scattering angle. It indicates that with the

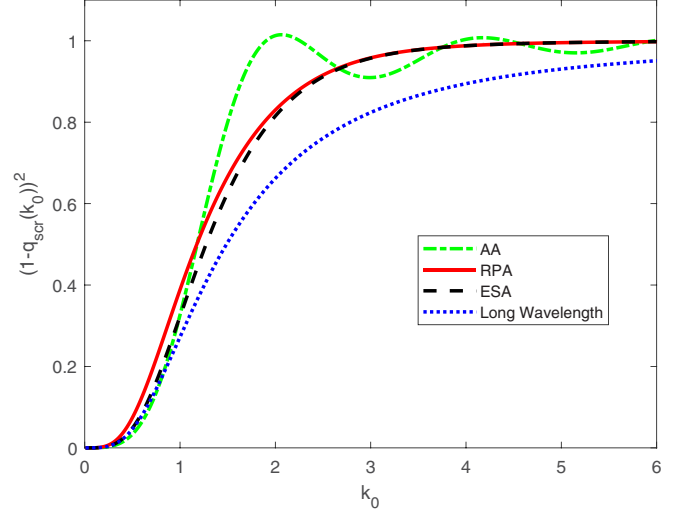


FIG. 1. Screening factor $[1 - q_{\text{scr}}(k)]^2$ for Al^{3+} plasma at $\rho = 2.7 \text{ g cm}^{-3}$ and $t = 10 \text{ eV}$. Dash-dotted green line: average-atom model; solid red line: random phase approximation; dashed black line: effective static approximation; and dotted blue line: long-wavelength formula.

accurate atomic wave functions, the AA model is able to bring more atomic-structural details to its screening factors.

III. RESULTS AND DISCUSSION

A. Free-electron contribution to IPD

To fully understand the influence of including dynamical effect and static LFC on the free-electron contribution to IPD [Eq. (7)] at WDM conditions, three different approaches are utilized to obtain static SF: the Debye-Hückel formula [Eq. (9)] and the dynamical SF approach [Eq. (10)] under RPA and ESA. Figure 2 provides an overview of corrections to the free-electron part of the IPD at WDM conditions ($0.5 \leq \Theta \leq 4.0$, $1.0 \leq r_s \leq 10.0$). As depicted in Fig. 2(a), the dynamical effect is manifested by comparing the IPD values calculated with the static SF from the Debye-Hückel model and from the RPA treatment, while the differences between the predictions evaluated by RPA and ESA represent the static LFC effect and are shown in Fig. 2(b). The combination of these two effects is summarized by a comparison between the DH and ESA results and is displayed in Fig. 2(c). For a better understanding and analysis of the results, associate static SFs from the DH, RPA, and ESA approaches are also calculated and shown in Fig. 3 for $r_s = 1.0$ with $\Theta = 0.5$ (upper panel) and with $\Theta = 4.0$ (lower panel) as well as in Fig. 4 for $r_s = 10.0$ with $\Theta = 0.5$ (upper panel) and with $\Theta = 4.0$ (lower panel).

As can be seen in Fig. 2(a), dynamical effect has a significant and nontrivial influence on free-electron contribution to IPD. At high-density condition ($n_e > 10^{23} \text{ cm}^{-3}$), dynamical effect reduces the free-electron part of the IPD by up to 20% from zero with decreasing temperature. On the other hand, in the low-density region ($n_e < 10^{23} \text{ cm}^{-3}$), dynamical effect raises the free-electron part of the IPD by up to 10% with decreasing temperature, and the increment tends to zero quickly upon raising the temperature. For a deeper comprehension of this behavior, we have to return to the involved

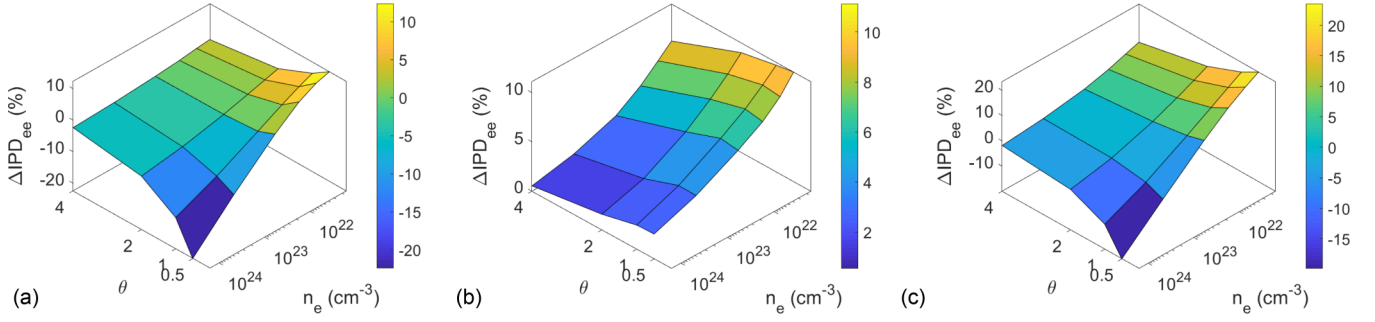


FIG. 2. Corrections to the free-electron part of IPD [Eq. (7)] at WDM conditions ($0.5 \leq \Theta \leq 4.0$, $1.0 \leq r_s \leq 10.0$) by introducing different effects: (a) the consideration of dynamical SF under RPA instead of the Debye-Hückel formula [Eq. (9)]; (b) the introduction of static LFC in calculating dynamical SF; (c) a combination of these two effects.

static SFs for more details. Figure 3 shows the comparison of the static SFs at $r_s = 1.0$ ($n_e = 1.6 \times 10^{24} \text{ cm}^{-3}$) with two different temperatures. In the case of low temperature (upper panel), the Debye-Hückel model generally overestimates the long-range part ($k/k_F < 1.0$) of SFs, which plays the most significant role in the IPD calculation, because the main contribution to the IPD comes from the small- k_0 region due to the quadratic dependence of the integrand $S_{ee}^0(k_0)/k_0^2$ in Eq. (7). This explains the reason why DH overestimates the free-electron contribution to IPD in the high-density region. At high temperature (lower panel in Fig. 3), both methods agree well with each other, therefore the reduction goes to zero as obtained before. A comparison of SFs for a lower density at $r_s = 10.0$ ($n_e = 1.6 \times 10^{21} \text{ cm}^{-3}$) is displayed in Fig. 4. As shown in the upper panel, in the low temperature ($\Theta = 0.5$) DH underestimates the medium-short-range part ($k/k_F > 0.5$) of SFs due to the lack of dynamical correlation in short-range interaction, and finally leads to the underestimation of the free-electron contribution to the IPD in the low-density region.

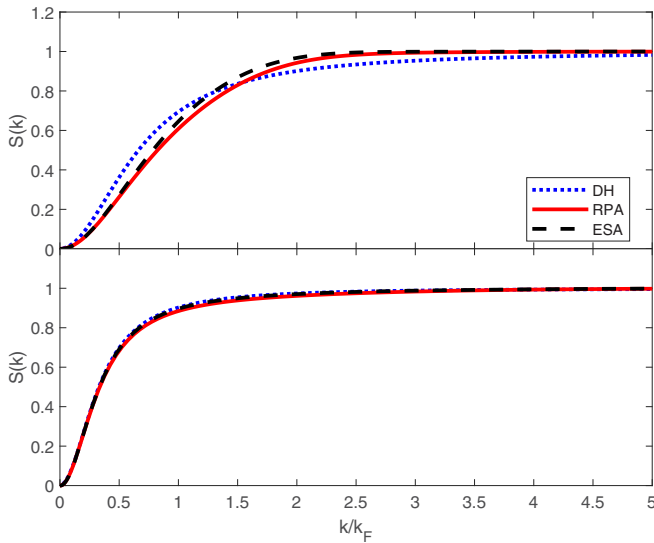


FIG. 3. Different approximations of static SFs at $r_s = 1.0$ and $\Theta = 0.5$ (upper panel) and $\Theta = 4.0$ (lower panel). Dotted blue line: Debye-Hückel formula (Eq. 9); solid red line: dynamical SF approach [Eq. (10)] under RPA; dashed black line: dynamical SF approach under ESA.

With the increase of the electron degeneracy parameter, the distinction between different SFs becomes less abundant, as is depicted in the lower panel of Fig. 4. In the case of nearly ideal plasmas, the static SFs predicted by other models are all converged into the DH results similar to the case shown in the lower panel of Fig. 3 and hence the Debye-Hückel limit is recovered.

The effect of static LFC on the free-electron part of the IPD is summarized in Fig. 2(b). Situations are quite different from what has been observed in the case of dynamical effect: static LFC poses a positive correction in the entire WDM region. The free-electron contribution to IPD is not sensitive to the static LFC at high-density condition ($n_e > 10^{23} \text{ cm}^{-3}$), and the overall correction is less than 2%. This conclusion can be reflected in Fig. 3, where only a slightly larger value of SF in the ESA approach is observed in comparison with RPA. With decreasing of the electron density, this deviation gradually increases and finally reaches 10%. From Fig. 4 it is obvious to conclude that ESA offers a better description for the long-range part of the SF and for the correlation-induced maximum (coupling peak) at $q \approx 2.2q_F$. At higher temperature, SF based on ESA still manifests a non-negligible

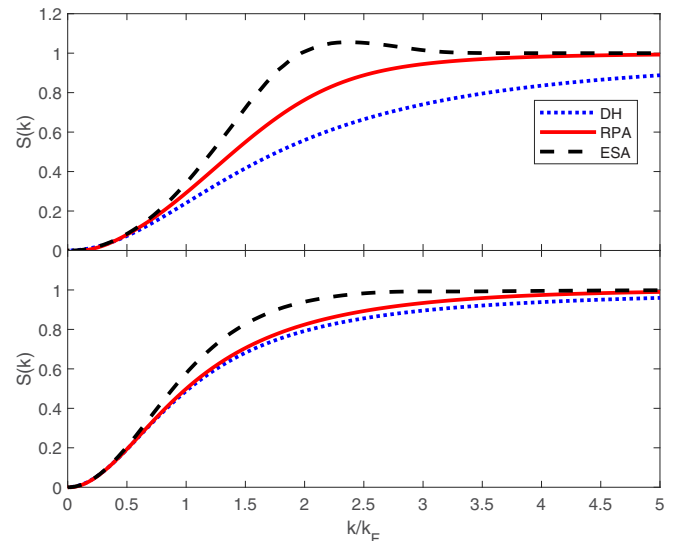


FIG. 4. Different approximations of static SFs at $r_s = 10.0$ and $\Theta = 0.5$ (upper panel) and $\Theta = 4.0$ (lower panel).

TABLE I. IPD values for Fe plasma at low density (case a), high density (case b), and Mg (case c), respectively. z_α represents the most probable ionic charge state in current condition. The experimental data are taken from Ref. [60].

Case	z_α	n_e (cm ⁻³)	t (eV)	Expt. (eV)	SP (eV)	EK (eV)	SF (eV)
a	Fe ¹⁷⁺	4.0×10^{22}	194.8	...	77.1	145.4	76.2
	Fe ¹⁷⁺	3.1×10^{22}	181.8	...	70.8	133.7	69.2
	Fe ¹⁷⁺	2.0×10^{22}	169.8	...	60.6	114.9	56.9
	Fe ¹⁷⁺	7.1×10^{21}	164.6	...	42.1	81.4	35.5
b	Fe ⁸⁺	1.6×10^{24}	25.1	...	175.2	254.7	334.8
	Fe ⁹⁺	1.6×10^{24}	50.1	...	187.1	281.8	291.4
	Fe ¹¹⁺	1.6×10^{24}	110.2	...	210.2	336.0	287.7
c	Mg ⁷⁺	3.0×10^{23}	75.0	132	89.3	129.9	131.9

correction at the long-medium-range part ($0.5 < k/k_F < 4.0$), which explains the slow decay of the correction upon increasing temperature.

Figure 2(c) shows the direct summation of results in Figs. 2(a) and 2(b). In the high-density region ($n_e > 10^{23}$ cm⁻³), the dynamical effect dominates the correction. The static LFC cancels out a small part of the dynamical effect, yet the overall shape of correction looks similar to that in Fig. 2(a) and the IPD is reduced up to 15% within this area. At low-density conditions ($n_e < 10^{23}$ cm⁻³), the total correction gets enhanced by the union of these two effects and reaches up to 20% at $n_e = 1.6 \times 10^{21}$ cm⁻³ and $\Theta = 0.5$. Figure 2 also provides the validity region (at WDM conditions, i.e., $0.5 \leq \Theta \leq 4.0$, $1.0 \leq r_s \leq 10.0$) for the application of commonly proposed DH and RPA methods. RPA is able to obtain reliable results (with errors up to 2%) at $n_e > 10^{23}$ cm⁻³, and the local field effect starts to manifest itself at a lower density. Calculations within the Debye-Hückel model become accurate only when $n_e < 10^{23}$ cm⁻³ and $\Theta \geq 2.0$.

B. Low-density region

As we can see in Fig. 2(c), the correction to the free-electron part of the IPD by dynamical effect and static LFC reaches its maximum at $r_s = 10.0$ ($n_e = 1.6 \times 10^{21}$ cm⁻³) and $\Theta = 0.5$ ($t = 0.25$ eV). However, pressure ionization does not dominate at low-density condition; the whole system is still close to an isolated state. The majority of our familiar materials and chemical elements (even hydrogen) is barely ionized at this low temperature. Therefore, we perform our IPD calculation for the low-density case on another case which exerts a tremendous interest. The experiments were performed by Bailey *et al.* [61], where wavelength-resolved iron opacity was measured at electron temperatures of 1.0–2.3 million K and electron densities of $(0.7\text{--}4.0) \times 10^{22}$ cm⁻³, and the results are 30–400% higher than predicted.

Full versions of the IPD calculations [Eq. (6)] are used here to calculate the aforementioned temperature-density points. In fact, such condition corresponds to the moderate coupling and nondegenerate ($\Theta > 45$) plasma. The dynamical correlation as well as the quantum exchange effect of free electrons are of no great importance. In this case, the DH and also the RPA model provide sufficient descriptions on the behavior of free electrons. On the other hand, for the screened ionic part, the multi-ion molecular dynamics (MIMD) simulation [62] is performed to obtain the ionic SF as well as the charge state

distribution of the plasma systems. Based on the free-electron density distribution from the simulation, the corresponding screening function can be obtained via Eq. (17).

Calculations on IPD with different models (SP, EK, and this work, SF) for the four related temperature-density points are presented in case (a) of Table I. According to our MIMD simulations, Fe¹⁷⁺ is the most probable ionic charge state at these conditions, and we take it as an example. It is commonly believed that the SP model has a good performance in this regime, and it can be seen from the table that our results generally agree well with the predictions by the SP model. The EK model, however, appears to seriously overestimate the IPD up to twice as much as the value of the other methods.

To investigate the dependence of IPD on the charge state z_α , a further calculation is performed on Fe plasma at a fixed free-electron density of $n_e = 3.1 \times 10^{22}$ cm⁻³ and temperature of $t = 181.834$ eV. It can be clearly seen from the upper panel of Fig. 5, there is an excellent agreement between our method and the SP model, while the EK model generally

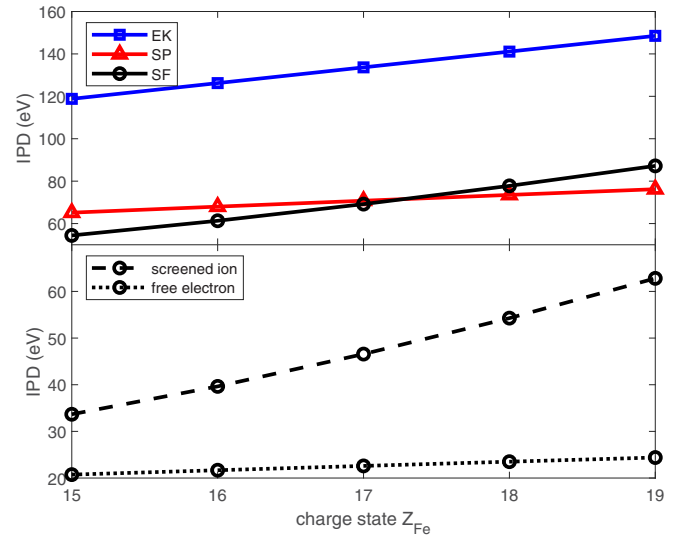


FIG. 5. IPD (upper panel) and its components (lower panel) as a function of different charge state Fe^{n+} at a fixed free-electron density of 3.1×10^{22} cm⁻³ and temperature of 181.834 eV. The averaged ionic SF and free-electron density distribution are obtained from MIMD simulation, and the corresponding screening function is calculated via Eq. (17). The SF of free electrons is computed via Eqs. (10)–(12) with RPA.

deviates more than twice the value of the other methods. Separate contributions from electrons and ions are further presented in the lower panel of Fig. 5. The screened ionic contribution is much larger than the free-electron one; this “counterintuitive” result is mainly due to the fact that the most significant contribution, i.e., electron-ion screening effect, is included in the screened ionic one, as explained in Sec. II C. Such difference between screened-ion and free-electron IPD strengthens itself as the charge of the ion under investigation increases. In addition, a nonlinear dependence of IPD values on the charge state is observed. The reason is that, besides the linear dependence on the charge state ($z_\alpha + 1$) contained in the coefficient of Eq. (8), the impurity-perturber coupling strength Γ_α also slightly depends on the charge number z_α . The unification of both dependencies results in a superlinear scaling behavior for the relation between IPD and the charge state.

C. High-density region

In the high-density regime, the reduction of free-electron IPD (up to 20%) as a direct consequence of the dynamical effect was highlighted in Sec. III A. In this section, we still take Fe plasma as an example to perform the full version of IPD calculation at a fixed free-electron density of $1.6 \times 10^{24} \text{ cm}^{-3}$ and varying degeneracies. MIMD simulations further reveal that there is only one charge state Fe^{8+} and Fe^{9+} within the plasma at $\Theta = 0.5$ and 1.0, respectively. This is mainly due to the fact that pressure ionization dominates at these relatively high-density and low-temperature conditions. Temperature-induced ionization and the corresponding charge state distribution, on the other hand, only starts to manifest itself at $\Theta = 2.0$.

Firstly, calculations for temperatures of 25.1, 50.1, and 100.2 eV are performed, where the most probable charge states are Fe^{8+} , Fe^{9+} , and Fe^{11+} , respectively. The results are shown in case (b) of Table I. As we can see from the table, the SP model seems to underestimate the IPD up to over 100 eV in this case. Apparently, for Fe^{8+} and Fe^{9+} ions, our method as well as the EK model predict higher IPD values than the corresponding ionization potential [63] (233.6 eV for Fe^{8+} and 262.1 eV for Fe^{9+}) in the isolated system. This means that these ions are pressure ionized to higher charge states, which is contradictory to the MIMD simulation results. We note that a possible reason could be the lack of consideration of inner-shell screening which might become important in high-density plasmas if the interionic distance is comparable with the size of ions/atoms.

Similar to the case of low-density conditions, IPD calculations in the high-density regime for different charge states Fe^{n+} at a fixed free-electron density of $1.6 \times 10^{24} \text{ cm}^{-3}$ and temperature of 100.2 eV are also implemented. The upper panel of Fig. 6 illustrates that our method is generally located between the EK and the SP model, and seems to be closer to the EK one. The green dashed line represents the IP in isolated condition as a function of different charge states, and the IPD above this line corresponds to a negative IP which indicates the ionization of a related ion. Due to the lack of an accurate description of the ion-ion correlation effect, the SP model usually underestimates the IPD values in the high-density regime.

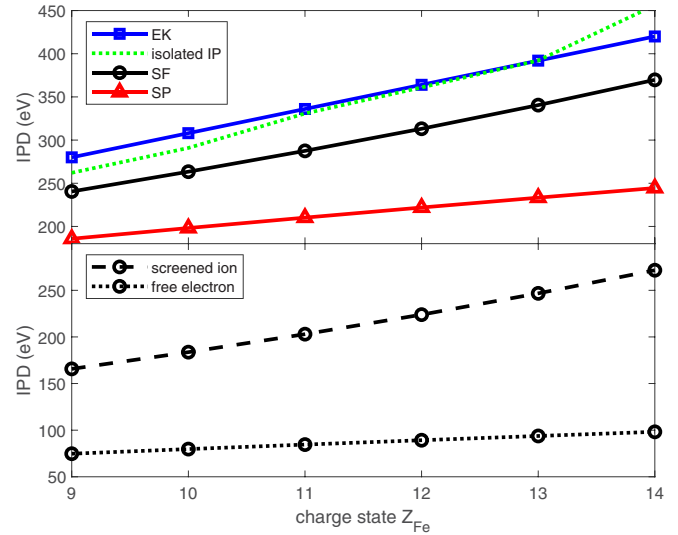


FIG. 6. IPD (upper panel) and its component (lower panel) as a function of different charge states Fe^{n+} at a fixed free-electron density $n_e = 1.6 \times 10^{24} \text{ cm}^{-3}$ and temperature $t = 100.2 \text{ eV}$. The corresponding IPs in the isolated condition are also included in the upper panel as a green dashed line. The averaged ionic SF and free-electron density distribution are obtained from MIMD simulation, and the corresponding screening function is calculated via Eq. (17). The SF of free electrons is computed via Eqs. (10)–(12) with ESA.

While the calculation of the EK model shows that the majority of charge states (Fe^{9+} to Fe^{13+}) would be pressure ionized according to the upper panel in Fig. 6. Consequently, a higher most probable charge state as well as a large averaged charge state are predicted by the EK model, which poses a conflicting result with the MIMD simulations. Within our approach, the ionic SF is applied to accurately describe the correlation effect between ions, thus more reasonable IPD values are obtained for plasmas under warm dense conditions.

The last set of calculations is performed on Mg plasma, where the experiment data [60] of IPD is available at warm dense condition with $n_e = 3.0 \times 10^{23} \text{ cm}^{-3}$ and $t = 75 \text{ eV}$. As shown in case (c) of Table I, our IPD calculation matches perfectly with the experiment result, and the EK model has good estimation as well. The SP model, however, underestimates the IPD value over 40 eV. It can be concluded that the results displayed in Table I, in Fig. 5, and in Fig. 6 clearly demonstrate the validity of our IPD method in the wide density-temperature region.

IV. CONCLUSION

In the present work, we incorporated the machine learning representation of static LFC based on PIMC within our IPD framework through the connection of dynamical SFs, therefore dynamical exchange-correlation effects are completely included compared to previous work. As demonstrated in the research, the dynamical screening effect has a significant influence on the IPD and hence on the ionization balance in warm dense systems. The consequence including dynamical effects through dynamical SF with the static LFC has been explicitly displayed in a two-step calculation within our

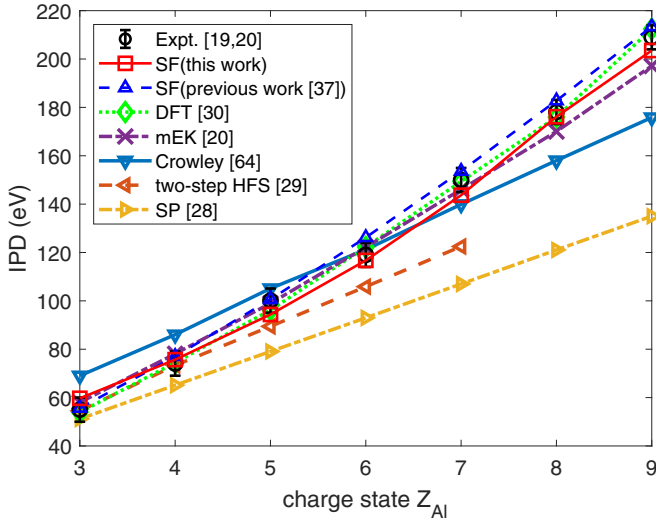


FIG. 7. IPD for aluminum plasma as a function of different charge state Al^{n+} at solid density and electron temperature $T_e = 100\text{eV}$. Shown are experimental results taken from Ref. [19,20] with an error bar $\pm 5\text{eV}$, in comparison to our predictions (previous work and this work) and other theoretical models.

approach. Firstly, the dynamical effect was investigated by applying the dynamical SF evaluated from the RPA dielectric function. Subsequently, the LFC effect was studied by replacing the RPA dielectric function by the modified response function obtained with static LFC for the determination of the dynamical SF. Our calculations on IPD at WDM conditions ($0.5 \leq \Theta \leq 4.0$, $1.0 \leq r_s \leq 10.0$) demonstrate that in the high-density condition, dynamical description within the RPA provides a sufficient description on the behavior of free electrons and leads to a reduction up to 20% compared to the static description with the Debye-Hückel model, whereas the correction induced by the static LFC effect on the free-electron part of IPD is less than 2%. Upon decreasing the electron density (with fixed degeneracy), the coupling between free electrons grows and the LFC effect starts to manifest itself. In particular, the dynamical SF calculated with static LFC is more reasonable to describe the short-range correlation as well as the coupling peak (around $k \approx 2.2k_F$) of the electronic subsystem. The combination of both effects will pose a nontrivial correction on the free-electron part of the IPD under strongly degenerated conditions from -18% at high-density regimes to 20% at low-density regions.

For the screened ionic part, MIMD simulation was performed to obtain the the ionic SF as well as the charge state distribution of the plasma systems. Based on the free-electron density distribution from MIMD simulation, the corresponding screening function is obtained via Eq. (17). As applications of the proposed method, warm dense Fe plasmas and Mg plasma were studied in detail. Full versions of IPD calculations on Fe plasmas were performed at a wide range of density-temperature conditions, and excellent agreements are obtained with the commonly employed SP or EK model at their corresponding valid regimes. Additionally, our IPD calculation matches quite well with the experiment result performed on Mg plasma at $n_e = 3.0 \times 10^{23} \text{ cm}^{-3}$ and $t = 75 \text{ eV}$.

ACKNOWLEDGMENTS

This work was supported by Science Challenge Project No. TZ2018005 and by the National Natural Science Foundation of China under Grants No. 11774322, No. 11974424, and No. 12004356.

APPENDIX: COMPARISON WITH OTHER THEORETICAL PREDICTIONS

Since a new screening factor [Eq. (17)], static LFC, as well as the dynamical effects [Eqs. (10)–(12)] are incorporated into the IPD framework as described in the main text, a combination of theoretical modeling with *ab initio* simulation is realized compared with the previous approach proposed in Ref. [37]. In order to provide a comprehensive assessment on the validity and robustness of the approach presented in this work, we show a detailed comparison of our numerical predictions with the LCLS experimental data [19,20], the results displayed in Ref. [37], and other theoretical results [28–30,64] for solid-density aluminum in Fig. 7.

On the one hand, the experimental observations are well reproduced by our quantum-statistical-based approach and other predictions including the modified EK model [20] and the finite-temperature density functional theory method [30], whereas the SP model [28], the two-step Hartree-Fock-Slater approach [29], and the IPD calculations by Crowley [64] seem to be less satisfying. On the other hand, a reasonable correction (less than 5%) to our previous results is obtained in Fig. 7, as the current condition situates on a trivial area in Fig. 2(c).

[1] P. Mazzotta, G. Mazzitelli, S. Colafrancesco, and N. Vittorio, Ionization balance for optically thin plasmas: Rate coefficients for all atoms and ions of the elements H to Ni*, *Astron. Astrophys. Suppl. Ser.* **133**, 403 (1998).
 [2] G. Mazzitelli and M. Mattioli, Ionization balance for optically thin plasmas: Rate coefficients for Cu, Zn, Ga, and Ge ions, *At. Data Nucl. Data* **82**, 313 (2002).
 [3] J. Zeng, Y. Li, Y. Hou, C. Gao, and J. Yuan, Ionization potential depression and ionization balance in dense carbon plasma under solar and stellar interior conditions, *Astron. Astrophys.* **644**, A92 (2020).

[4] W. Lotz, Electron-impact ionization cross-sections and ionization rate coefficients for atoms and ions from hydrogen to calcium, *Z. Phys.* **216**, 241 (1968).
 [5] P. O. Danis, D. E. Karr, D. G. Westmoreland, M. C. Piton, D. I. Christie, P. A. Clay, S. H. Kable, and R. G. Gilbert, Measurement of propagation rate coefficients using pulsed-laser polymerization and matrix-assisted laser desorption/ionization mass spectrometry, *Macromolecules* **26**, 6684 (1993).
 [6] S. N. Nahar and A. K. Pradhan, and H. L. Zhang, Electron-ion recombination rate coefficients and photoionization cross sections for astrophysically abundant elements IV. Relativistic

- calculations for C IV and C V for UV and x-ray modeling, *Astrophys. J. Suppl. S.* **131**, 375 (2000).
- [7] G. S. Voronov, A practical fit formula for ionization rate coefficients of atoms and ions by electron impact: $Z = 1-28$, *At. Data Nucl. Data* **65**, 1 (2017).
- [8] É. Falize, A. Ravasio, B. Loupiau, A. Dizière, C. D. Gregory, C. Michaut, C. Busschaert, C. Cavet, and M. Koenig, High-energy density laboratory astrophysics studies of accretion shocks in magnetic cataclysmic variables, *High Energy Density Phys.* **8**, 1 (2012).
- [9] S. H. Glenzer and R. Redmer, X-ray Thomson scattering in high energy density plasmas, *Rev. Mod. Phys.* **81**, 1625 (2009).
- [10] R. P. Drake, Focus on high energy density physics, *Phys. Plasma* **16**, 055501 (2009).
- [11] H. J. Lee, P. Neumayer, J. Castor, T. Doppner, R. W. Falcone, C. Fortmann, B. A. Hammel, A. L. Kritcher, O. L. Landen, R. W. Lee, D. D. Meyerhofer, D. H. Munro, R. Redmer, S. P. Regan, S. Weber, and S. H. Glenzer, X-Ray Thomson-Scattering Measurements of Density and Temperature in Shock-Compressed Beryllium, *Phys. Rev. Lett.* **102**, 115001 (2009).
- [12] E. G. Saiz, G. Gregori, F. Y. Khattak, J. Kohanoff, S. Sahoo, G. S. Naz, S. Bandyopadhyay, M. Notley, R. L. Weber, and D. Riley, Evidence of Short-Range Screening in Shock-Compressed Aluminum Plasma, *Phys. Rev. Lett.* **101**, 075003 (2008).
- [13] M. D. Knudson, M. P. Desjarlais, R. W. Lemke, T. R. Mattsson, M. French, N. Nettelmann, and R. Redmer, Probing the Interiors of the Ice Giants: Shock Compression of Water to 700 GPa and $3.8\text{g}/\text{cm}^3$, *Phys. Rev. Lett.* **108**, 091102 (2012).
- [14] N. Nettelmann, R. Redmer, and D. Blaschke, Warm dense matter in giant planets and exoplanets, *Phys. Part. Nuclei* **39**, 1122 (2008).
- [15] S. H. Glenzer, B. J. MacGowan, P. Michel, N. B. Meezan, L. J. Suter, S. N. Dixit, J. L. Kline, G. A. Kyrala, D. K. Bradley, and D. A. Callahan, Symmetric inertial confinement fusion implosions at ultra-high laser energies, *Science* **327**, 1228 (2010).
- [16] J. Lindl, Development of the indirect-drive approach to inertial confinement fusion and the target physics basis for ignition and gain, *Phys. Plasmas* **2**, 3933 (1995).
- [17] P. B. Corkum, Laser-generated plasmas: Probing plasma dynamics, *Nat. Photonics* **2**, 272 (2008).
- [18] R. R. Faustlin, T. Bornath, T. Doppner, S. Dusterer, E. Forster, C. Fortmann, S. H. Glenzer, S. Gode, G. Gregori, R. Irsig *et al.*, Observation of Ultrafast Nonequilibrium Collective Dynamics in Warm Dense Hydrogen, *Phys. Rev. Lett.* **104**, 125002 (2010).
- [19] O. Ciricosta, S. M. Vinko, B. Barbrel, D. S. Rackstraw, T. R. Preston, T. Burian, J. Chalupsky, B. I. Cho, H. K. Chung, G. L. Dakovski *et al.*, Measurements of continuum lowering in solid-density plasmas created from elements and compounds, *Nat. Commun.* **7**, 11713 (2016).
- [20] O. Ciricosta, S. M. Vinko, H. K. Chung, B. I. Cho, C. R. Brown, T. Burian, J. Chalupsky, K. Engelhorn, R. W. Falcone, C. Graves *et al.*, Direct Measurements of the Ionization Potential Depression in a Dense Plasma, *Phys. Rev. Lett.* **109**, 065002 (2012).
- [21] D. Kraus, D. A. Chapman, A. L. Kritcher, R. A. Baggott, B. Bachmann, G. W. Collins, S. H. Glenzer, J. A. Hawreliak, D. H. Kalantar, O. L. Landen, T. Ma, S. Le Pape, J. Nilsen, D. C. Swift, P. Neumayer, R. W. Falcone, D. O. Gericke, and T. Doppner, X-ray scattering measurements on imploding CH spheres at the national ignition facility, *Phys. Rev. E* **94**, 011202(R) (2016).
- [22] D. J. Hoarty, P. Allan, S. F. James, C. R. Brown, L. M. Hobbs, M. P. Hill, J. W. Harris, J. Morton, M. G. Brookes, R. Shepherd, J. Dunn, H. Chen, E. Von Marley, P. Beiersdorfer, H. K. Chung, R. W. Lee, G. Brown, and J. Emig, Observations of the Effect of Ionization-Potential Depression in Hot Dense Plasma, *Phys. Rev. Lett.* **110**, 265003 (2013).
- [23] L. B. Fletcher, A. L. Kritcher, A. Pak, T. Ma, T. Doppner, C. Fortmann, L. Divol, O. S. Jones, O. L. Landen, H. A. Scott, J. Vorberger, D. A. Chapman, D. O. Gericke, B. A. Mattern, G. T. Seidler, G. Gregori, R. W. Falcone, and S. H. Glenzer, Observations of Continuum Depression in Warm Dense Matter with X-Ray Thomson Scattering, *Phys. Rev. Lett.* **112**, 145004 (2014).
- [24] T. R. Preston, S. M. Vinko, O. Ciricosta, H. K. Chung, R. W. Lee, and J. S. Wark, The effects of ionization potential depression on the spectra emitted by hot dense aluminium plasmas, *High Energy Density Phys.* **9**, 258 (2013).
- [25] S. M. Vinko, O. Ciricosta, B. I. Cho, K. Engelhorn, H. K. Chung, C. R. Brown, T. Burian, J. Chalupsky, R. W. Falcone, C. Graves *et al.*, Creation and diagnosis of a solid-density plasma with an x-ray free-electron laser, *Nature (London)* **482**, 59 (2012).
- [26] B. I. Cho, K. Engelhorn, S. M. Vinko, H. K. Chung, O. Ciricosta, D. S. Rackstraw, R. W. Falcone, C. R. Brown, T. Burian, J. Chalupsky *et al.*, Resonant $K\alpha$ Spectroscopy of Solid-Density Aluminum Plasmas, *Phys. Rev. Lett.* **109**, 245003 (2012).
- [27] G. Ecker and W. Kröll, Lowering of the ionization energy for a plasma in thermodynamic equilibrium, *Phys. Fluids* **6**, 62 (1963).
- [28] J. C. Stewart and K. D. Pyatt, Jr., Lowering of ionization potentials in plasmas, *Astrophys. J.* **144**, 1203 (1966).
- [29] S. K. Son, R. Thiele, Z. Jurek, B. Ziája, and R. Santra, Quantum-Mechanical Calculation of Ionization-Potential Lowering in Dense Plasmas, *Phys. Rev. X* **4**, 031004 (2014).
- [30] S. M. Vinko, O. Ciricosta, and J. S. Wark, Density functional theory calculations of continuum lowering in strongly coupled plasmas, *Nat. Commun.* **5**, 3533 (2014).
- [31] S. X. Hu, Continuum Lowering and Fermi-Surface Rising in Strongly Coupled and Degenerate Plasmas, *Phys. Rev. Lett.* **119**, 065001 (2017).
- [32] M. Stransky, Monte Carlo simulations of ionization potential depression in dense plasmas, *Phys. Plasmas* **23**, 012708 (2016).
- [33] C. A. Iglesias and P. A. Sterne, Fluctuations and the ionization potential in dense plasmas, *High Energy Density Phys.* **9**, 103 (2013).
- [34] F. B. Rosmej, Ionization potential depression in an atomic-solid-plasma picture, *J. Phys. B: At., Mol. Opt. Phys.* **51**, 09LT01 (2018).
- [35] J. Zeng, Y. Li, C. Gao, and J. Yuan, Screening potential and continuum lowering in a dense plasma under solar-interior conditions, *Astron. Astrophys.* **634**, A117 (2020).
- [36] R. Jin, M. M. Abdullah, Z. Jurek, R. Santra, and S. K. Son, Transient ionization potential depression in nonthermal dense plasmas at high x-ray intensity, *Phys. Rev. E* **103**, 023203 (2021).

- [37] C. Lin, G. Ropke, W. D. Kraeft, and H. Reinholz, Ionization-potential depression and dynamical structure factor in dense plasmas, *Phys. Rev. E* **96**, 013202 (2017).
- [38] G. Ropke, D. Blaschke, T. Doppner, C. Lin, W. D. Kraeft, R. Redmer, and H. Reinholz, Ionization potential depression and Pauli blocking in degenerate plasmas at extreme densities, *Phys. Rev. E* **99**, 033201 (2019).
- [39] C. Lin, Quantum statistical approach for ionization potential depression in multi-component dense plasmas, *Phys. Plasmas* **26**, 122707 (2019).
- [40] T. Dornheim, S. Groth, and M. Bonitz, The uniform electron gas at warm dense matter conditions, *Phys. Rep.* **744**, 1 (2018).
- [41] E. W. Brown, B. K. Clark, J. L. Dubois, and D. M. Ceperley, Path Integral Monte Carlo Simulation of the Warm-Dense Homogeneous Electron Gas, *Phys. Rev. Lett.* **110**, 146405 (2013).
- [42] T. Dornheim, S. Groth, T. Sjöstrom, F. D. Malone, W. M. Foulkes, and M. Bonitz, *Ab Initio* Quantum Monte Carlo Simulation of the Warm Dense Electron Gas in the Thermodynamic Limit, *Phys. Rev. Lett.* **117**, 156403 (2016).
- [43] S. Groth, T. Dornheim, T. Sjöstrom, F. D. Malone, W. M. C. Foulkes, and M. Bonitz, *Ab Initio* Exchange-Correlation Free Energy of the Uniform Electron Gas at Warm Dense Matter Conditions, *Phys. Rev. Lett.* **119**, 135001 (2017).
- [44] S. Groth, T. Dornheim, and J. Vorberger, *Ab initio* path integral Monte Carlo approach to the static and dynamic density response of the uniform electron gas, *Phys. Rev. B* **99**, 235122 (2019).
- [45] T. Dornheim, A. Cangi, K. Ramakrishna, M. Bohme, S. Tanaka, and J. Vorberger, Effective Static Approximation: A Fast and Reliable Tool for Warm-Dense Matter Theory, *Phys. Rev. Lett.* **125**, 235001 (2020).
- [46] P. Hamann, T. Dornheim, J. Vorberger, Z. A. Moldabekov, and M. Bonitz, Dynamic properties of the warm dense electron gas based on *ab initio* path integral Monte Carlo simulations, *Phys. Rev. B* **102**, 125150 (2020).
- [47] T. Dornheim, S. Groth, and M. Bonitz, *Ab initio* results for the static structure factor of the warm dense electron gas, *Contrib. Plasma Phys.* **57**, 468 (2017).
- [48] T. Dornheim, S. Groth, J. Vorberger, and M. Bonitz, *Ab Initio* Path Integral Monte Carlo Results for the Dynamic Structure Factor of Correlated Electrons: From the Electron Liquid to Warm Dense Matter, *Phys. Rev. Lett.* **121**, 255001 (2018).
- [49] T. Dornheim, J. Vorberger, S. Groth, N. Hoffmann, Z. A. Moldabekov, and M. Bonitz, The static local field correction of the warm dense electron gas: An *ab initio* path integral Monte Carlo study and machine learning representation, *J. Chem. Phys.* **151**, 194104 (2019).
- [50] K. S. Singwi, M. P. Tosi, R. H. Land, and A. Sjölander, Electron correlations at metallic densities, *Phys. Rev.* **176**, 589 (1968).
- [51] S. Tanaka and S. Ichimaru, Thermodynamics and correlational properties of finite-temperature electron liquids in the Singwi-Tosi-Land-Sjölander approximation, *J. Phys. Soc. Jpn.* **55**, 2278 (1986).
- [52] T. Sjöstrom and J. Dufty, Uniform electron gas at finite temperatures, *Phys. Rev. B* **88**, 115123 (2013).
- [53] M. Corradini, R. Del Sole, G. Onida, and M. Palumbo, Analytical expressions for the local-field factor $G(q)$ and the exchange-correlation kernel $K_{xc}(r)$ of the homogeneous electron gas, *Phys. Rev. B* **57**, 14569 (1998).
- [54] R. Bredow, Th. Bornath, W. D. Kraeft, and R. Redmer, Hypernetted chain calculations for multi-component and nonequilibrium plasmas, *Contrib. Plasma Phys.* **53**, 276 (2013).
- [55] D. Saumon, C. E. Starrett, J. D. Kress, and J. Cléroutin, The quantum hypernetted chain model of warm dense matter, *High Energy Density Phys.* **8**, 150 (2012).
- [56] Y. Hou, R. Bredow, J. Yuan, and R. Redmer, Average-atom model combined with the hypernetted chain approximation applied to warm dense matter, *Phys. Rev. E* **91**, 033114 (2015).
- [57] J. Yuan, Self-consistent average-atom scheme for electronic structure of hot and dense plasmas of mixture, *Phys. Rev. E* **66**, 047401 (2002).
- [58] Y. Hou, F. Jin, and J. Yuan, Influence of the electronic energy level broadening on the ionization of atoms in hot and dense plasmas: An average atom model demonstration, *Phys. Plasmas* **13**, 093301 (2006).
- [59] Y. Hou and J. Yuan, Alternative ion-ion pair-potential model applied to molecular dynamics simulations of hot and dense plasmas: Al and Fe as examples, *Phys. Rev. E* **79**, 016402 (2009).
- [60] Q. Y. van den Berg, E. V. Fernandez-Tello, T. Burian, J. Chalupsky, H. K. Chung, O. Ciricosta, G. L. Dakovski, V. Hajkova, P. Hollebon, L. Juha *et al.*, Clocking Femtosecond Collisional Dynamics Via Resonant X-Ray Spectroscopy, *Phys. Rev. Lett.* **120**, 055002 (2018).
- [61] J. E. Bailey, T. Nagayama, G. P. Loisel, G. A. Rochau, C. Blancard, J. Colgan, P. Cosse, G. Faussurier, C. J. Fontes, F. Gilleron *et al.*, A higher-than-predicted measurement of iron opacity at solar interior temperatures, *Nature (London)* **517**, 56 (2015).
- [62] Y. Fu, Y. Hou, D. Kang, C. Gao, F. Jin, and J. Yuan, Multi-charge-state molecular dynamics and self-diffusion coefficient in the warm dense matter regime, *Phys. Plasmas* **25**, 012701 (2018).
- [63] A. Kramida, Yu. Ralchenko, J. Reader, and NIST ASD, NIST Atomic Spectra Database (ver. 5.8). Available online at <https://physics.nist.gov/asd>, accessed April 1, 2021 (National Institute of Standards and Technology, Gaithersburg, MD, 2020).
- [64] B. J. B. Crowley, Continuum lowering—A new perspective, *High Energy Density Phys.* **13**, 84 (2014).